Model dependence in the photoproduction of kaons from protons and deuterons

Oren V. Maxwell
Department of Physics, Florida International University, University Park, Miami, Florida 33199, USA
(Received 6 May 2004; published 28 October 2004)

The reactions $\gamma p \to K^+\Lambda$ and $\gamma d \to K^+\Lambda n$ have been investigated over the energy range from $E_\gamma = 1.0$ GeV to $E_\gamma = 1.8$ GeV in a tree-level effective Lagrangian model that incorporates most of the well-established resonances of spins $\frac{1}{2}$ and $\frac{3}{2}$ below 1.9 GeV. Several sets of values for the resonance couplings are generated by fitting empirical cross section curves for the proton reaction at three different energies. Results obtained with a number of these fits are then presented for the cross sections and several single polarization observables for both reactions. The deuteron reaction is treated within the impulse approximation with final state interactions incorporated by means of a nonrelativistic overlap integral in momentum space. We explore the dependences of the calculated quantities on several facets of the model, including the particular resonance fit employed, the treatment of the spin $\frac{3}{2}$ resonance propagator, the prescription used for the resonance widths, and for the deuteron reaction, the final state interaction and deuteron wave function employed. We find that for neither reaction are the cross sections very sensitive to any of the model details. The polarization observables, on the other hand, are quite sensitive to certain model details, particularly to the resonance model employed and to the prescription used for the resonance widths. In general the polarization observables in the proton reaction are more sensitive to model details than the polarization observables in the deuteron reaction. The calculated deuteron observables are not strongly dependent on either the final state interaction or the deuteron wave function employed.

DOI: 10.1103/PhysRevC.70.044612 PACS number(s): 25.10.+s, 25.20.Lj, 13.60.−r

I. INTRODUCTION

The electromagnetic production of strangeness from protons has been of interest in the nuclear community for almost 40 years but, until recently, has suffered from a lack of high quality data, particularly polarization data. Despite this, numerous theoretical approaches have been developed based on effective Lagrangian models [1–10], quark models [11–14], and SU(3) chiral dynamics [15,16]. Recent polarization data from both photoproduction experiments [17,18] and electroproduction experiments [19,20] provide stringent constraints on these models and on future theoretical work. Indeed, the beam polarization asymmetries measured in the most recent photoproduction experiment do not agree with the predictions of a recent Lagrangian model calculation [18], even though that calculation incorporates the SAPHIR polarization data in its fit of the resonance coupling strengths.

In contrast with electromagnetic strangeness production from the proton, comparatively little effort has been directed toward the electromagnetic production of strangeness from heavier targets. Renard and Renard [21] first examined kaon photoproduction from the deuteron in the late 1960s. Later studies of this reaction have concentrated primarily on the role of final state interactions between the outgoing baryons [22–24]. There were a few photoproduction [25] and electroproduction [26] experiments carried out with deuteron targets in the 1970s, but these were mainly concerned with the extraction of the cross section for Σ^- production from the neutron. Moreover, the photoproduction experiments involved the use of quite high energy photon beams at SLAC. More recent work at TJNAF is expected to yield data of much greater abundance and quality, but as yet there is no published data from these experiments.

In view of the range and quality of forthcoming data for electromagnetic strangeness production and the wide variety of theoretical work that addresses these reactions, it is perhaps of interest to reexamine some model dependent aspects of the calculations within the context of a particular model. Here we concentrate on the photoproduction of Λ's using an effective Lagrangian model simliar to that introduced in Ref. [1]. For reactions involving proton targets, the main uncertainties connected with this model arise from the choice of resonances to include in the model and the extent to which the couplings of these resonances can be fixed by the existing data. There is additional model dependence, however, associated with the forms adopted for the intermediate baryon propagators and electromagnetic vertices, especially for higher spin resonances, and with the treatment of the energy and momentum dependence of the *s*-channel resonance widths. In the case of deuteron targets, the treatment of final state interactions and the deuteron wave function are further sources of model dependence.

In this work, we present a variety of results for both proton and deuteron targets in an effort to explore these various types of model dependence. In the case of deuteron targets, we employ the impulse approximation supplemented with final state interactions. Since our calculations are meant to be exploratory in nature, we content ourselves with a nonrelativistic deuteron wave function. The main effect that the incorporation of relativity has on the deuteron wave function is to introduce small *p*-wave components arising from the lower components of the Dirac spinors. The effect of these small *p*-wave components on kaon photoproduction was examined in Ref. [22] and found to be relatively unimportant.

The model employed for the proton reaction,

$$\gamma + p \to K^+ + \Lambda \tag{1}$$

consists of *s*-channel, *u*-channel, and *t*-channel contributions. These various contributions are discussed in detail in Sec. II,

where the set of resonances included in the model is enumerated and various options presented for the treatment of the spin $\frac{3}{2}$ propagator. This section also outlines two different prescriptions for the treatment of the *s*-channel resonance widths.

Within the impulse approximation, the incident photon in the deuteron reaction,

$$\gamma + d \rightarrow K^+ + \Lambda + n \tag{2}$$

must be absorbed by the proton, so that the same model that is employed to analyze the proton reaction can be used to examine the deuteron reaction as well. This is discussed in Sec. III, where a prescription is presented for the inclusion of final state interactions by means of an overlap integral in momentum space.

Results for both proton and deuteron targets are contained in Sec. IV. Here, we compare several fits to the proton data using different sets of resonances, different prescriptions for the spin $\frac{3}{2}$ propagator, and different resonance width prescriptions. The various fits are then used to calculate single polarization observables in the proton reaction and both cross sections and polarization observables in the deuteron reaction. We also study the dependence of the deuteron results on the input wave functions by employing three different potentials to generate the final state interactions and by using two different deuteron wave functions.

II. THE REACTION MODEL

Figure 1 displays the various contributions to reaction [1] that are included in the present work. In the *s*-channel, the Born contribution with an intermediate proton is supplemented by additional contributions involving the excitation of an intermediate nucleon resonance. Similarly, the *u*-channel Born terms are supplemented with contributions involving the excitation of intermediate hyperon resonances, while in the *t*-channel, contributions from both $K^\star(892)$ and $K1(1270)$ exchange are included.

A list of all the resonances incorporated in the present work is given in Table I. The spin-parity assignments in the third column have been taken from the particle data tables [27], while the symmetry assignments in column 4 are consistent with those used in SU(6) X O(3) analyses of spectra and decay rates [28,29]. Included in this table are all of the well-established resonances (those of three or four star status in the particle data tables) below 1.9 GeV that have spins of $\frac{1}{2}$ or $\frac{3}{2}$. The restriction to spins less than $\frac{5}{2}$ was imposed mainly for the sake of simplicity. There are not many well-established resonances below 1.9 GeV with spins larger than $\frac{3}{2}$ in any case, so that their exclusion should not qualitatively affect our results.

The impulse amplitudes depicted in Fig. 1 have the general form

$$\hat{T}_s = \sum_R \mathcal{V}_K^\dagger(p_K) D(p) \mathcal{V}_\gamma(p_\gamma), \tag{3}$$

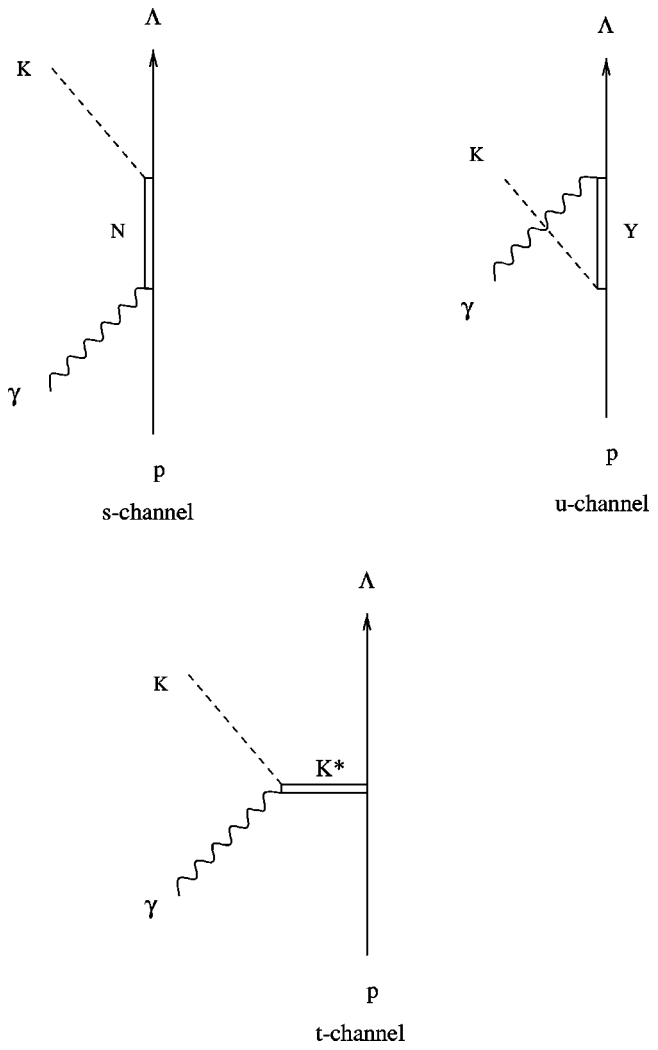

FIG. 1. Contributions to the amplitude for the reaction $\gamma p \rightarrow K^+\Lambda$.

$$\hat{T}_u = \sum_R \mathcal{V}_\gamma^\dagger(p_\gamma) D(p') \mathcal{V}_K(p_K), \tag{4}$$

and

$$\hat{T}_t = \sum_{K^\star} V_{\gamma K}^\dagger(p_\gamma, p_{K^\star}) D_{K^\star}(p_{K^\star}) \mathcal{V}_{p\Lambda}(p_{K^\star}), \tag{5}$$

where $p = p_\Lambda + p_K$ and $p' = p_\Lambda - p_\gamma$ are the intermediate 4-momenta in the *s*- and *u*-channel terms, respectively, and $p_{K^\star}$ is the kaon resonance 4-momentum in the *t*-channel term. The $\mathcal{V}$'s here denote electromagnetic and strong interaction vertex functions, while the *D*'s denote the propagators associated with the intermediate baryon and meson lines.

In the *t*-channel the vertex functions are given by the expressions

$$\mathcal{V}_{\gamma K}^\mu = \frac{g_{\gamma K K^\star}}{m_{sc}} \epsilon^{\mu\nu\rho\lambda} \epsilon_\nu p_{\gamma\rho} p_{K^\star\lambda} \tag{6}$$

and

$$\mathcal{V}^{\mu}_{p\Lambda} = \left(g^{V}_{p\Lambda K^{\star}} + \frac{g^{T}_{p\Lambda K^{\star}}}{m_p + m_\Lambda} \gamma \cdot p_{K^{\star}} \right) \gamma^{\mu} \tag{7}$$

for the $K^{\star}(892)$ resonance and

$$\mathcal{V}^{\mu}_{\gamma K} = \frac{g_{\gamma KK1}}{m_{sc}} (\epsilon \cdot p_{K1} p^{\mu}_{\gamma} - p_{\gamma} \cdot p_{K1} \epsilon^{\mu}) \tag{8}$$

and

$$\mathcal{V}^{\mu}_{p\Lambda} = \left(g^{V}_{p\Lambda K1} + \frac{g^{T}_{p\Lambda K1}}{m_p + m_\Lambda} \gamma \cdot p_{K1} \right) \gamma^{\mu} \gamma_5 \tag{9}$$

for the $K1(1270)$ resonance, where m_{sc} is a scaling mass that we set equal to 1000 MeV. The two kaon resonances have propagators of the same form,

$$D_{K^{\star}} = \frac{-g_{\mu\nu} + \dfrac{p_{K^{\star}\mu} p_{K^{\star}\nu}}{m^2_{K^{\star}}}}{p^2_{K^{\star}} - m^2_{K^{\star}} + i m_{K^{\star}} \Gamma_{K^{\star}}}, \tag{10}$$

where now the label $K^{\star}$ refers to either of the two resonances.

The vertex functions and propagators associated with the *s* and *u*-channels depend upon the spin and parity of the intermediate baryon line. For intermediate baryons of spin $\frac{1}{2}$, we employ the standard expression at the electromagnetic vertex and use the pseudoscalar coupling form at the meson vertex. This gives for positive parity baryons

$$\mathcal{V}_{K(1/2)^{+}}(p_K) = g \gamma_5 \tag{11}$$

and

$$\mathcal{V}_{\gamma(1/2)^{+}}(p_\gamma) = g_\gamma \epsilon_\mu i \sigma^{\mu\nu} (p_\gamma)_\nu, \tag{12}$$

with

$$g_\gamma = \frac{e\kappa}{2 m_B}, \tag{13}$$

where m_B is the proton mass in the *s*-channel and the Λ mass in the *u*-channel, and κ is defined by its relation to the transition magnetic moment,

$$\mu_T = \frac{e\kappa}{m_B + m_I}. \tag{14}$$

In the last expression m_I denotes the mass of the intermediate baryon. The corresponding expressions for negative parity baryons just have the γ_5 factor transposed from the meson vertex to the electromagnetic vertex. For intermediate proton states, there is an additional charge term,

$$\mathcal{V}_{charge}(p_\gamma) = e \gamma^{\mu} (p_\gamma)_\mu \tag{15}$$

that has to be added to the positive parity electromagnetic vertex above.

For the spin $\frac{1}{2}$ propagator, we employ a relativistic Breit-Wigner form,

TABLE I. Resonances included in the model.

Resonance	I	J^P	$SU(3)$
$N(1440)$	$1/2$	$1/2^+$	$^2 8$
$N(1520)$	$1/2$	$3/2^-$	$^2 8$
$N(1535)$	$1/2$	$1/2^-$	$^2 8$
$N(1650)$	$1/2$	$1/2^-$	$^4 8$
$N(1700)$	$1/2$	$3/2^-$	$^4 8$
$N(1710)$	$1/2$	$1/2^+$	$^2 8$
$N(1720)$	$1/2$	$3/2^+$	$^2 8$
$\Lambda(1405)$	0	$1/2^-$	$^2 1$
$\Lambda(1520)$	0	$3/2^-$	$^2 1$
$\Lambda(1600)$	0	$1/2^+$	$^2 8$
$\Lambda(1670)$	0	$1/2^-$	$^4 8$
$\Lambda(1690)$	0	$3/2^-$	$^2 8$
$\Lambda(1810)$	0	$1/2^+$	$^2 8$
$\Lambda(1890)$	0	$3/2^+$	$^2 8$
$\Sigma(1385)$	1	$3/2^+$	$^4 10$
$\Sigma(1660)$	1	$1/2^+$	$^2 8$
$\Sigma(1670)$	1	$3/2^-$	$^2 8$
$\Sigma(1750)$	1	$1/2^-$	$^2 10$

$$D^{1/2}(p) = \frac{\gamma \cdot p + m_I}{p^2 - m^2_I + i m_I \Gamma_I}, \tag{16}$$

where Γ_I is the width associated with the intermediate baryon in the *s*-channel and is zero in the *u*-channel. This form has been used in most of the previous photoproduction studies. However, Benmerrouche *et al.* have noted that Eq. (16) leads to inconsistent amplitudes in different partial waves and hence, violates unitarity [30]. Ideally, one should generate the imaginary part of the *t*-matrix self-consistently through a *K*-matrix approach; however, this would entail the solution of a large set of coupled channel equations that would complicate the analysis considerably.

There has been considerable discussion in the literature concerning the correct forms for the propagator and interaction vertices of spin $\frac{3}{2}$ baryons. On the baryon mass shell, the various prescriptions for the propagator reduce to the Rarita-Schwinger form, which is obtained by multiplying the spin $\frac{1}{2}$ propagator on the right by the projection operator

$$P_{\mu\nu} = g_{\mu\nu} - \frac{1}{3}\gamma_\mu \gamma_\nu + \frac{1}{3}\frac{p_\mu \gamma_\nu - p_\nu \gamma_\mu}{m_I} - \frac{2}{3}\frac{p_\mu p_\nu}{m^2_I}. \tag{17}$$

Off the mass shell, this form does not preserve gauge invariance. The authors of Ref. [1] attempted to restore gauge invariance by replacing the baryon masses in the expression above and the numerator of Eq. (16) by $\sqrt{s}$, but this yields a form that does not satisfy the differential equation defining the Green's function, as demonstrated in Ref. [30]. More recent work has shown that a full description of the off-shell structure of the spin $\frac{3}{2}$ propagator and interaction Lagrangians requires the incorporation of additional parameters [7,30,31]. In this work, we attempt to estimate the

model dependence associated with these parameters by comparing results obtained with two different forms for the propagator, the Rarita-Schwinger form (RS propagator) and the form employed in Ref. [1] (ABW propagator). We note that, aside from its failure to satisfy the differential equation defining the Green's function, the ABW propagator introduces unphysical singularities in the u-channel where $\sqrt{s}$ can vanish.

For the sake of simplicity, the forms employed here for the spin $\frac{3}{2}$ interaction vertices do not incorporate off-shell parameters. The positive parity interaction vertices are given by

$$\mathcal{V}^{\mu}_{K(3/2)^+}(p_K) = -\frac{g}{m_\pi} p_K^\mu \tag{18}$$

and

$$\mathcal{V}^{\mu}_{\gamma(3/2)^+}(p_\gamma) = \left[\frac{g_1}{2m_B}(\epsilon^\mu \gamma\cdot p_\gamma - p_\gamma^\mu \gamma\cdot\epsilon) + \frac{g_2}{4m_B^2}(\epsilon\cdot p_B p_\gamma^\mu - p_\gamma\cdot p_B \epsilon^\mu)\right]\gamma_5, \tag{19}$$

where p_B is the ground state baryon 4-momentum, and the factor m_π in the first expression makes g dimensionless. The negative parity vertices just have the γ_5 factor transposed from the electromagnetic vertex to the meson vertex.

A. Coupling strengths

To evaluate the various amplitudes discussed above, values are required for the products of the coupling strengths at the two interaction vertices. We adopt fixed values for the coupling strength products in the t-channel and in the Born contributions to the s and u-channels and then adjust the coupling strengths associated with the s and u-channel resonance contributions to fit the cross section data for reaction (1).

For the t-channel coupling products, we employ the values used in Ref. [6]. These are given by

$$g^V_{p\Lambda K^\star} g_{\gamma K K^\star} = -2.01,$$

$$g^T_{p\Lambda K^\star} g_{\gamma K K^\star} = 1.00,$$

$$g^V_{p\Lambda K1} g_{\gamma K K1} = 0.25,$$

$$g^T_{p\Lambda K1} g_{\gamma K K1} = 2.13. \tag{20}$$

The s and u-channel Born contributions involve the electromagnetic coupling parameters κ_p, κ_Λ, and $\kappa_{\Lambda\Sigma}$, defined by Eq. (14), and the strong interaction couplings $g_{\Lambda Kp}$ and $g_{\Sigma Kp}$. For the electromagnetic couplings, we use the values given in the particle data tables [27] with the exception of $\kappa_{\Lambda\Sigma}$ for which it was necessary to use a reduced value. The required strong interaction couplings can be deduced from the well established πN coupling strength using SU(3) symmetry [32], but this yields a value for $g_{\Lambda Kp}$ that is difficult to accommodate with experimental data. Instead, as in many other fits to strangeness photo and electroproduction data, we employ a value for this coupling that is substantially smaller than the SU(3) estimate. These considerations yield the s and u-channel Born coupling products

$$e\kappa_p g_{\Lambda Kp} = -2.88,$$

$$e\kappa_\Lambda g_{\Lambda Kp} = 0.75,$$

$$e\kappa_{\Lambda\Sigma} g_{\Sigma Kp} = 1.46, \tag{21}$$

where $e=0.3029$ is the electron charge in dimensionless units.

For the spin $\frac{1}{2}$ s and u-channel resonance contributions, we define the coupling strength products

$$F_{N^\star} = e\kappa_{pN^\star} g_{\Lambda K N^\star},$$

$$F_{\Lambda^\star} = e\kappa_{\Lambda\Lambda^\star} g_{\Lambda^\star K p},$$

$$F_{\Sigma^\star} = e\kappa_{\Lambda\Sigma^\star} g_{\Sigma^\star K p} \tag{22}$$

and for the spin $\frac{3}{2}$ resonance contributions, the products

$$G^1_{N^\star} = g_1^{pN^\star} g_{\Lambda K N^\star},$$

$$G^2_{N^\star} = g_2^{pN^\star} g_{\Lambda K N^\star},$$

$$G^1_{\Lambda^\star} = g_1^{\Lambda\Lambda^\star} g_{\Lambda^\star K p},$$

$$G^2_{\Lambda^\star} = g_2^{\Lambda\Lambda^\star} g_{\Lambda^\star K p},$$

$$G^1_{\Sigma^\star} = g_1^{\Lambda\Sigma^\star} g_{\Sigma^\star K p},$$

$$G^2_{\Sigma^\star} = g_2^{\Lambda\Sigma^\star} g_{\Sigma^\star K p}. \tag{23}$$

B. Resonance widths

In addition to the coupling strength products, we need values for the s-channel resonance widths to evaluate the reaction amplitudes depicted in Fig. 1. The low lying nucleon resonance widths are reasonably well known on the resonance mass shells but are generally required at positions far off the mass shells. In this work we compare results obtained with two different prescriptions for the energy and momentum dependence of the resonance widths.

The first prescription, which was introduced in Ref. [33] and which we term the full width model, involves a decomposition of the empirical on-shell width into partial widths for decay into particular two-body and multibody channels. In each such channel, the off-shell energy and momentum dependence is treated using an effective Lagrangian model with the required coupling strength adjusted to yield the empirical on-shell branching ratio for decay into that channel.

The two-body channels all involve the decay of a nucleon resonance into a pseudoscalar meson and a spin $\frac{1}{2}$ baryon. In

TABLE II. $N^\star$ resonance on-shell branching ratios.

	Two body channels			Three body channels		
Resonance	$N\pi$	$N\eta$	ΛK	$N\rho$	$N\sigma$	$\Delta(1232)\pi$
$N(1440)$	0.65			0.10		0.25
$N(1520)$	0.55			0.20	0.05	0.20
$N(1535)$	0.45	0.50		0.03	0.02	
$N(1650)$	0.75	0.06	0.06	0.08		0.05
$N(1700)$	0.10	0.017		0.063	0.22	0.60
$N(1710)$	0.15	0.01	0.15		0.26	0.43
$N(1720)$	0.15	0.012	0.07	0.768		

the resonance rest frame, the widths for these decays are given by

$$\Gamma\left(\frac{1}{2}^P \rightarrow \frac{1}{2}^+ + 0^-\right) = \frac{f^2}{4\pi}\frac{p}{\sqrt{s}}[E_B - \eta_P m_B] \tag{24}$$

for spin $\frac{1}{2}$ resonances and by

$$\Gamma\left(\frac{3}{2}^P \rightarrow \frac{1}{2}^+ + 0^-\right) = \frac{1}{12\pi}\frac{f^2}{m_\pi^2}\frac{p^3}{\sqrt{s}}[E_B + \eta_P m_B], \tag{25}$$

for spin $\frac{3}{2}$ resonances, where P specifies the resonance parity, p is the channel momentum, E_B is the energy of the baryon decay product, and η_P is +1 or −1 for even or odd parity resonances, respectively. Below the threshold for a particular channel, the partial width for decay into that channel is set equal to zero. At higher energies, decay channels not available at the on-shell position may open up. Since we have no method for estimating the branching ratios into these channels, we simply ignore them. The intermediate baryon propagators are significantly reduced away from the on-shell positions, so this omission should not be important.

That part of the on-shell decay width not accounted for by two-body channels is assigned to multibody channels. These multibody channels are treated approximately as two-body decays into either a stable spin $\frac{1}{2}$ baryon and a meson resonance or a stable pseudoscalar meson and a baryon resonance. In particular, for the low lying nucleon resonances, we include decays into $N\rho$, $N\sigma$, and $\Delta(1232)\pi$ channels. For some of these channels, there exist empirical branching ratios with large error bars [27]. After adding the corresponding widths to the two-body widths, any remaining width still not accounted for is assigned to whatever other channels are open for that resonance. The resulting branching ratios for all the $N^\star$ resonances considered in this work are listed in Table II.

For fixed decay product masses, width expressions for channels involving vector mesons or spin $\frac{3}{2}$ baryons are given in Ref. [33]. This reference also provides a method, which we employ here, for taking into account the fact that the mass of an unstable decay product is not fixed, but distributed over a finite range. Briefly, this method requires the replacement of the unstable decay product mass in the width expression by a variable mass and then the integration of the product of the phase space factor in the width expression and a Breit-Wigner distribution function. Details are given in Ref. [33].

TABLE III. Parameters in the Λn interaction.

	Singlet parameters			
	U_0	α_0	W_0	β_0
Model A	167.34	1.100	246.80	0.82
Model B	373.94	0.790	246.80	0.82
Model C	131.49	1.095	246.80	0.82
	Triplet parameters			
	U_1	α_1	W_1	β_1
Model A	132.42	1.100	181.68	0.82
Model B	144.14	1.059	181.68	0.82
Model C	189.60	0.964	181.68	0.82

To test the sensitivity of the calculated observables to the width prescription, we also make use of a second, greatly simplified width prescription, which we term the simplified width model. This second prescription makes use of the on-shell partial widths at all energies and momenta above threshold; i.e., the on-shell widths in each channel are used off shell as well, except that, as in the full model, the partial width is set equal to zero below the channel threshold.

C. Matrix elements and observables for the reaction $\gamma p \rightarrow K^+\Lambda$

The baryon matrix elements of the amplitudes given by Eqs. (3), (4), and (5) between an incident proton and an outgoing Λ all have the general structure

$$\overline{u}_{M_\Lambda}(p_\Lambda)\hat{T}u_{M_p}(p_p) = \overline{u}_{M_\Lambda}(p_\Lambda)[\hat{A} + \hat{B}\gamma_5 + \hat{C}\gamma^0 + \hat{D}\gamma^0\gamma_5]u_{M_p}(p_p), \tag{26}$$

where p_p and M_p are the 4-momentum and spin projection of the proton, and p_Λ and M_Λ the 4-momentum and spin projection of the Λ. For each amplitude, the operators $\hat{A}$, $\hat{B}$, $\hat{C}$ and $\hat{D}$ depend upon the spin and parity of the particular intermediate resonance considered. Detailed expressions for these operators can be found in the Appendix of Ref. [33].

Carrying out the Dirac algebra in Eq. (26) yields the equivalent Pauli form,

$$\begin{aligned}\overline{u}_{M_\Lambda}(p_\Lambda)\hat{T}u_{M_p}(p_p) &= N_\Lambda N_p \chi^\dagger_{M_\Lambda}[(\hat{A}+\hat{C}) + (\hat{B}+\hat{D})\boldsymbol{\sigma}\cdot\hat{\mathbf{p}}_p \\ &\quad + \boldsymbol{\sigma}\cdot\hat{\mathbf{p}}_\Lambda(\hat{D}-\hat{B}) + \boldsymbol{\sigma}\cdot\hat{\mathbf{p}}_\Lambda(\hat{C}-\hat{A})\boldsymbol{\sigma}\cdot\hat{\mathbf{p}}_p]\chi_{M_p},\end{aligned} \tag{27}$$

with

$$N = \sqrt{\frac{E+m}{2m}} \tag{28}$$

and

TABLE IV. Coupling constant products.

		Spin $\frac{1}{2}$ resonances					
		A	B	C	D	E	F
$N(1440)$	$F_{N\star}$	−6.301	−2.495	−4.134	−8.365	−0.140	−8.251
$N(1535)$	$F_{N\star}$	−0.210	1.497	0.057	−0.356	0.186	−0.375
$N(1650)$	$F_{N\star}$		−0.709				
$\Lambda(1405)$	$F_{\Lambda\star}$	2.331	4.774	3.171	0.557	3.161	−0.309
$\Lambda(1600)$	$F_{\Lambda\star}$	−1.720	0.496	−3.612	1.813	0.855	−1.504
$\Lambda(1670)$	$F_{\Lambda\star}$	0.0073	0.0073		0.0073		
$\Lambda(1810)$	$F_{\Lambda\star}$					−2.804	
$\Sigma(1660)$	$F_{\Sigma\star}$	−3.465	−3.465		−3.465		
$\Sigma(1750)$	$F_{\Sigma\star}$	0.0014	−0.934	0.794	−0.904	1.192	0.091
		Spin $\frac{3}{2}$ resonances					
		A	B	C	D	E	F
$N(1520)$	$G^1_{N\star}$	0.027	0.079	0.082	0.079	0.062	−0.275
	$G^2_{N\star}$						
$N(1700)$	$G^1_{N\star}$	0.0051	−0.0075	0.024	−0.021	−0.0031	0.012
	$G^2_{N\star}$	−0.0006	−0.0005	0.0062	0.0010	0.034	−0.038
$N(1720)$	$G^1_{N\star}$	0.020	0.023	−0.010	0.031	−0.0018	0.026
	$G^2_{N\star}$						
$\Lambda(1690)$	$G^1_{\Lambda\star}$	0.319	0.319			0.551	
	$G^2_{\Lambda\star}$					−0.110	
$\Lambda(1890)$	$G^1_{\Lambda\star}$	1.493	1.493	1.029		1.029	
	$G^2_{\Lambda\star}$	−1.173	−1.173	−0.617		−0.617	
$\Sigma(1385)$	$G^1_{\Sigma\star}$	−0.422	−0.601	−0.233		−0.391	
	$G^2_{\Sigma\star}$	−0.069	−0.958	−1.339		−1.223	
$\Sigma(1670)$	$G^1_{\Sigma\star}$	0.601	0.221	0.414		−0.255	
	$G^2_{\Sigma\star}$	2.256	2.283	0.618		−0.114	

$$\hat{p} = \frac{\mathbf{p}}{E+m}. \tag{29}$$

This last expression can be further reduced analytically, but the procedure is rather tedious. Instead, Eq. (27) is evaluated numerically.

Equation (26) can also be evaluated numerically without recourse to a Pauli reduction. We have generated a code to accomplish this and checked that the results agree with the numerical evaluation of Eq. (27). This not only confirms the accuracy of the numerical codes, but also provides a check on the Dirac algebra.

In terms of these matrix elements, the unpolarized differential cross section for reaction (1) is given in the center of mass (c.m.) by

$$\frac{d\sigma}{d\Omega} = \frac{1}{(2\pi)^2}\frac{m_p m_\Lambda p_F}{4E_\gamma s}\frac{1}{4}\sum_{spins}|\langle F|\hat{T}|I\rangle|^2, \tag{30}$$

where p_F and s are the outgoing 3-momentum and squared total energy in the c.m., and E_γ is the incident photon energy.

In addition to the unpolarized cross section, we have also obtained results for the hyperon polarization asymmetry P, the polarized photon beam asymmetry Σ, and the polarized proton target asymmetry T defined by

$$P = \frac{d\sigma^+_\Lambda - d\sigma^-_\Lambda}{d\sigma^+_\Lambda + d\sigma^-_\Lambda}, \tag{31}$$

$$\Sigma = \frac{d\sigma^\perp_\gamma - d\sigma^\parallel_\gamma}{d\sigma^\perp_\gamma + d\sigma^\parallel_\gamma}, \tag{32}$$

and

$$T = \frac{d\sigma^+_p - d\sigma^-_p}{d\sigma^+_p + d\sigma^-_p}, \tag{33}$$

where the superscripts $^+$ and $^-$ refer to spin projections above and below the scattering plane, i.e., along the positive and negative y axes, respectively, and the superscripts $\perp$ and $\parallel$ refer to photon polarizations perpendicular and parallel to the scattering plane, respectively.

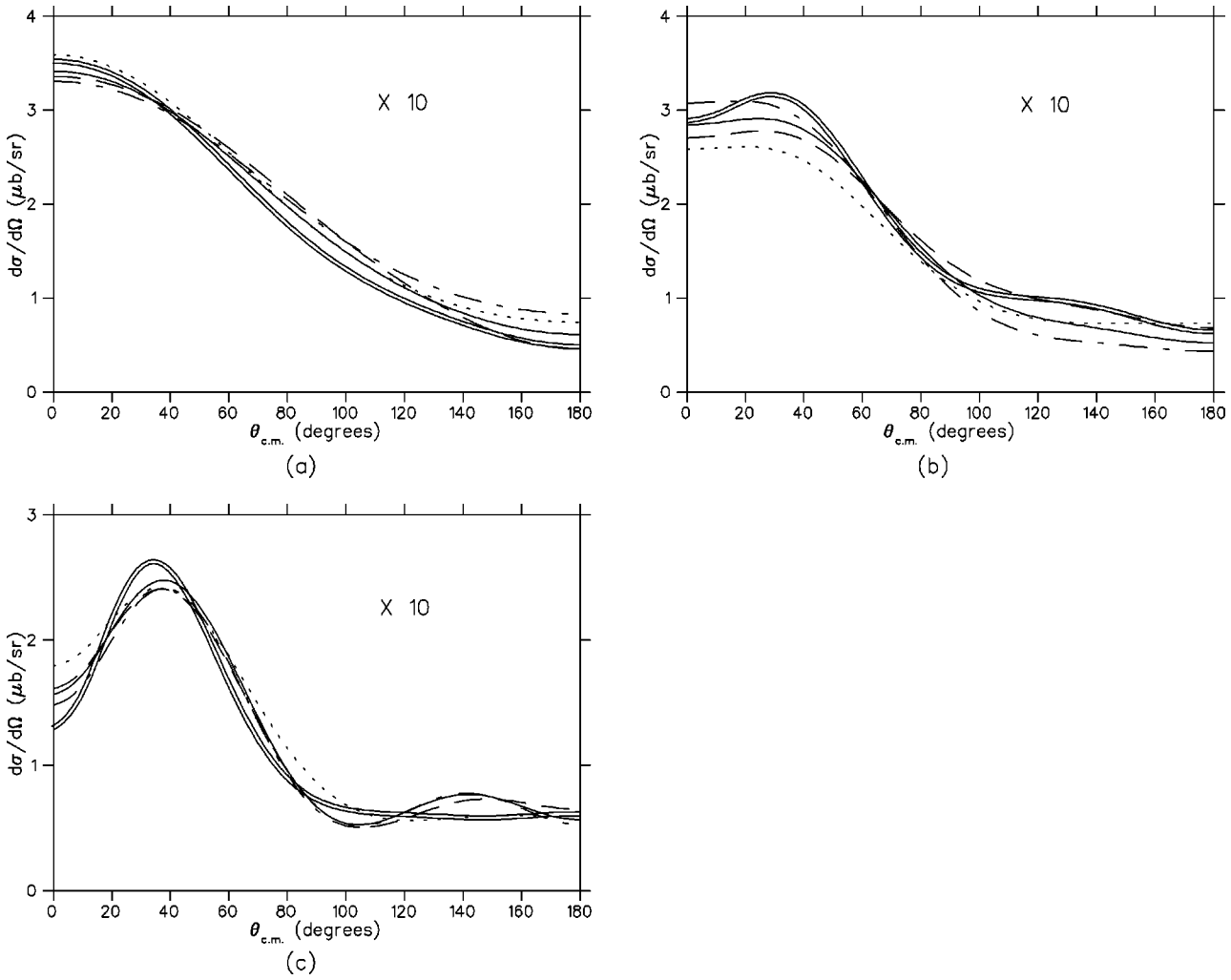

FIG. 2. Differential cross sections for the reaction $\gamma p \to K^+\Lambda$ at (a) E_γ=1.1 GeV, (b) E_γ=1.4 GeV, and (c) E_γ=1.7 GeV. The solid curves were obtained with fit A, the dashed curves with fit B, the dot-dashed curves with fit C, and the dotted curves with fit D, as described in the text. The double solid curves are empirical fits from Ref. [34].

III. THE REACTION $\gamma d \to K^+\Lambda n$

A. Matrix elements and observables with no final state interaction

Within the impulse approximation for reaction (2), the incident photon absorption and the outgoing kaon emission occur on the same baryon line, so that the reaction amplitude is identical to that given previously for a proton target. However, in contrast with the proton reaction, the matrix element for reaction (2) must be evaluated between two-body baryon states. This is most readily accomplished in momentum space in the rest frame of the deuteron.

The initial deuteron state consists of the product of an isospin factor and a spin-spatial wave function,

$$\Psi_M(\mathbf{p}) = |(pn)I=0\rangle \Phi_M(\mathbf{p}), \tag{34}$$

where M and $\mathbf{p}$ are the deuteron spin projection and relative 3-momentum, and

$$|(pn)I=0\rangle = \frac{1}{\sqrt{2}}(|pn\rangle - |np\rangle). \tag{35}$$

The two terms on the right side of the last expression yield identical matrix elements that can be accounted for by multiplying the reaction amplitude discussed previously by a factor two. Combined with the inverse $\sqrt{2}$ above, this yields an overall factor $\sqrt{2}$ in the deuteron matrix elements as compared with the proton matrix elements. Nonrelativistically, the function Φ_M can be further decomposed into products of spin and spatial wave functions,

$$\Phi_M(\mathbf{p}) = \sum_{M_S} \psi_{M,M_S}(\mathbf{p})|1M_S\rangle \tag{36}$$

with

$$|1M_S\rangle = \sum_{M_p,M_n} \left(\frac{1}{2}M_p\frac{1}{2}M_n|1M_S\right)\chi_{M_p}\chi_{M_n} \tag{37}$$

and

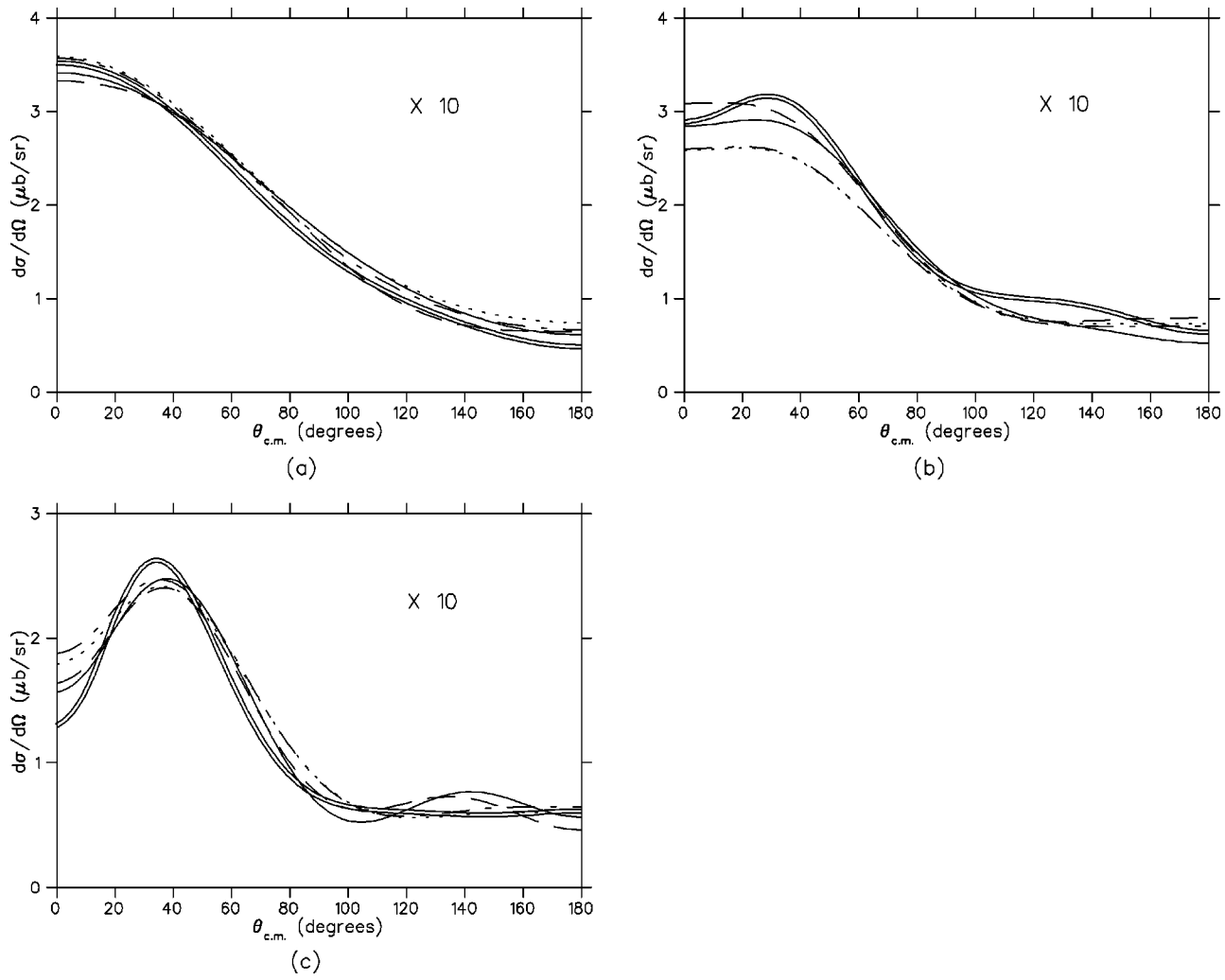

FIG. 3. Differential cross sections for the reaction $\gamma p \rightarrow K^+\Lambda$ at the same incident photon energies as in Fig. 2. The solid curves were obtained with fit A, the dashed curves with fit E, the dotted curves with fit D, and the dot-dashed curves with fit F, as described in the text. The double solid curves are empirical fits from Ref. [34].

$$\psi_{M,M_S}(\mathbf{p}) = \sum_{L=0,2} (LM - M_S 1 M_S | 1M) \tilde{\phi}_L(p) Y_{LM-M_S}(\theta_p, \phi_p), \tag{38}$$

where

$$\tilde{\phi}_L(p) = \sqrt{\frac{2}{\pi}} i^L \int_0^\infty r^2 \phi_L(r) j_L(pr) dr \tag{39}$$

is the radial part of the deuteron wave function in momentum space. To assess the sensitivity of the deuteron model to the initial state employed, we compare results obtained with two different deuteron wave functions, one based on the Reid nucleon-nucleon (NN) potential and the other based on the Paris NN potential.

In the absence of final state correlations, the matrix element for reaction (2) can be simply expressed in terms of the wave function defined above and the matrix element for reaction (1). In particular,

$$\langle F|\hat{T}|I\rangle_d = \sqrt{(2\pi)^3 2m_d}\, \mathcal{T}_{M_\Lambda M_{nF} M}(\mathbf{p}), \tag{40}$$

with

$$\mathcal{T}_{M_\Lambda M_{nF} M}(\mathbf{p}) = \sum_{M_S} \left(\frac{1}{2} M_S - M_{nF} \frac{1}{2} M_{nF} | 1 M_S \right) \psi_{M,M_S}(\mathbf{p}) \overline{u}_{M_\Lambda}(p_\Lambda) \times \hat{T} u_{M_S - M_{nF}}(p_p)\, \delta(p_{nF} - p_{nI}), \tag{41}$$

where the subscripts *nI* and *nF* refer to the initial and final neutron states, $\mathbf{p} = \mathbf{p_p} = -\mathbf{p}_{nF}$ in the deuteron rest frame, and the factor containing the deuteron mass m_d in Eq. (40) is a normalization factor.

In terms of this matrix element, the unpolarized differential cross section for reaction (2) is given in the deuteron rest frame by

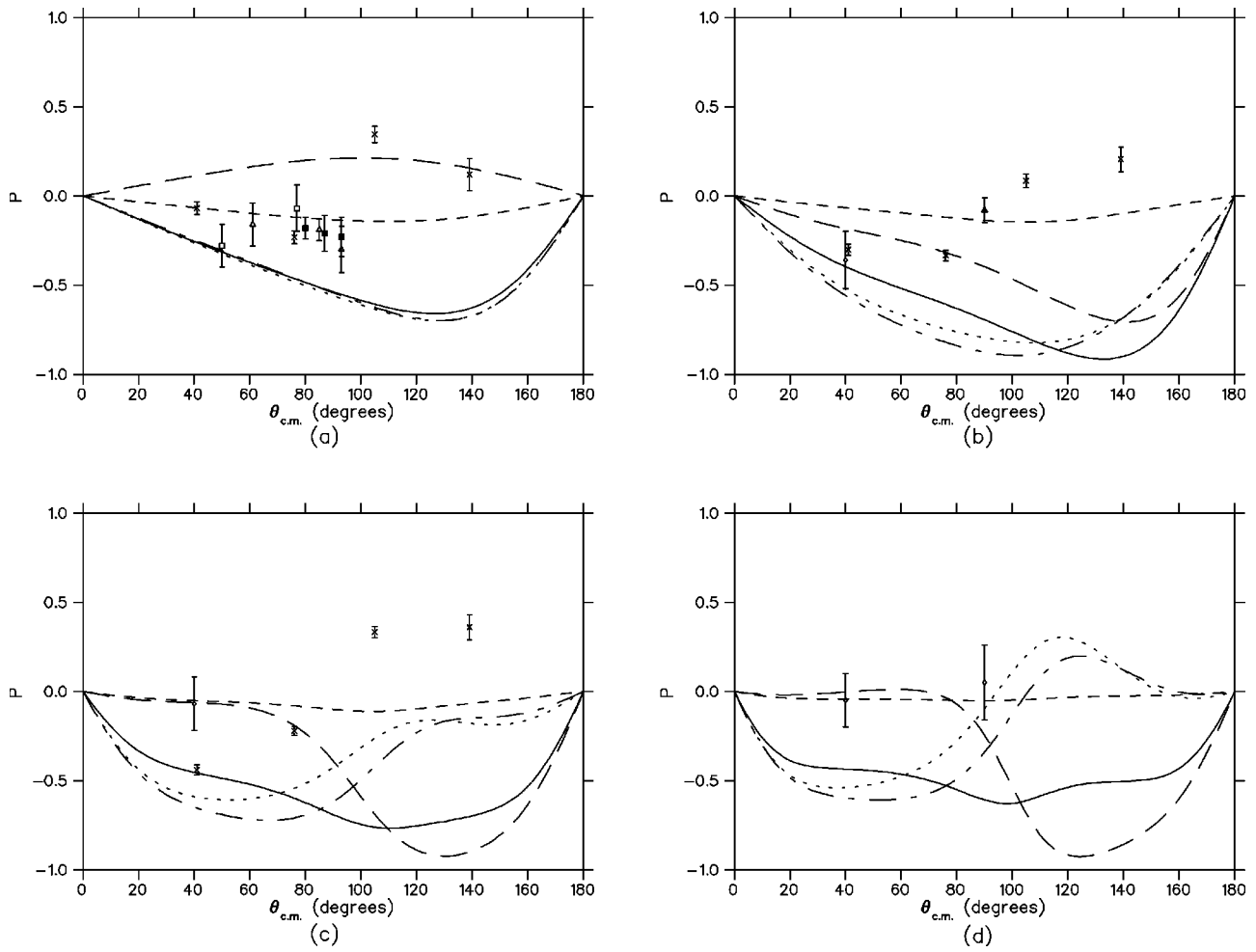

FIG. 4. Hyperon polarization asymmetry for the reaction $\gamma p \to K^+\Lambda$ at (a) E_γ=1.0 GeV, (b) E_γ=1.25 GeV, (c) E_γ=1.55 GeV, and (d) E_γ=1.7 GeV. The solid curves were obtained with fit A, the long dashed curves with fit B, the short dashed curves with fit E, the dotted curves with fit D, and the dot-dashed curves with fit F, as described in the text. The data points are from Ref. [35] (solid squares), Ref. [36] (open triangles), Ref. [37] (open squares), Ref. [38] (solid triangles), Ref. [39] (open diamonds), and Ref. [17] (crosses).

$$\frac{d^5\sigma}{dp_K d\Omega_K d\Omega_\Lambda} = \frac{1}{12}\frac{1}{(2\pi)^2}\frac{m_\Lambda m_n p_\Lambda p_K^2}{E_B E_K E_\gamma}\gamma(\theta_\Lambda)\sum_{spins}|\langle F|\hat{T}|I\rangle_d|^2, \tag{42}$$

with

$$\gamma^{-1} = \left[1 - \frac{E_\Lambda P_B}{E_B p_\Lambda}\cos(\theta_\Lambda)\right], \tag{43}$$

where E_B and $\mathbf{P_B}$ are the total outgoing baryon energy and 3-momentum in the deuteron rest frame, and θ_Λ is the angle between the $\mathbf{p_\Lambda}$ and $\mathbf{P_B}$. Results have also been obtained for the hyperon polarization asymmetry P defined by Eq. (31) and the polarized photon beam asymmetry defined by Eq. (32).

B. Inclusion of the final state interaction

The interaction between the neutron and the Λ in the final state is incorporated by means of a nonrelativistic overlap integral,

$$\mathcal{M}_{M_\Lambda M_{nF} M}(\mathbf{p}) = \sum_{M'_\Lambda M'_{nF}}\int\frac{d^3q}{(2\pi)^{3/2}}\Psi_{M_\Lambda M_{nF} M'_\Lambda M'_{nF}}(\mathbf{p},\mathbf{q}) \times \mathcal{T}_{M'_\Lambda M'_{nF} M}(\mathbf{q}), \tag{44}$$

which is substituted into Eq. (40) in place of Eq. (41). The quantity Ψ here is essentially the three dimensional Fourier transform of the Λn final state wave function. It is defined by the expression

$$\Psi_{M_\Lambda M_{nF} M'_\Lambda M'_{nF}}(\mathbf{p},\mathbf{q}) = \sum_{S=0,1}\left(\frac{1}{2}M_\Lambda\frac{1}{2}M_{nF}|SM_S\right) \times\left(\frac{1}{2}M'_\Lambda\frac{1}{2}M'_{nF}|SM_S\right)\psi_S(\mathbf{p},\mathbf{q}), \tag{45}$$

with

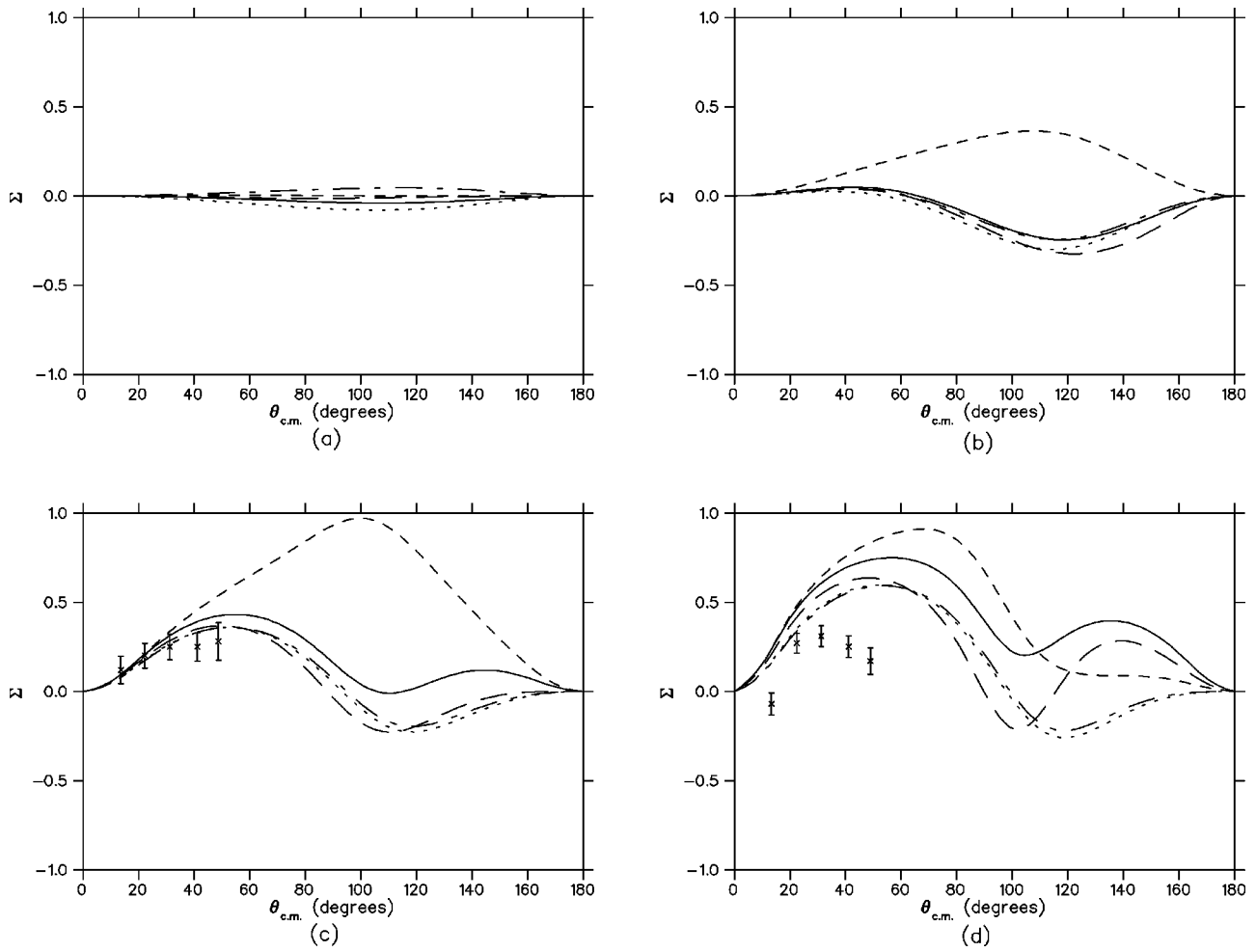

FIG. 5. Polarized photon beam asymmetry for the reaction $\gamma p \to K^+\Lambda$ at (a) E_γ=1.0 GeV, (b) E_γ=1.25 GeV, (c) E_γ=1.55 GeV, and (d) E_γ=1.75 GeV. Identification of curves as in Fig. 4. The data points are from Ref. [18].

$$\psi_S(\mathbf{p},\mathbf{q}) = \int \frac{d^3r}{(2\pi)^{3/2}} \exp(i\mathbf{q}\cdot\mathbf{r})\phi_S^*(\mathbf{p},\mathbf{r}) = \sqrt{\frac{2}{\pi}}\sum_\ell (2\ell+1)R_{\ell S}(p,q)P_\ell(\cos\theta_{pq}), \quad (46)$$

where θ_{pq} is the angle between the vectors $\mathbf{p}$ and $\mathbf{q}$, and

$$R_{\ell S}(p,q) = \int_0^\infty r^2 dr \frac{u_{\ell S}^*(p,r)}{r} j_\ell(qr) \quad (47)$$

is the overlap of the Λn radial wave function, $u_{\ell S}/r$, with the plane wave radial wave function, j_ℓ.

To represent the Λn potential, we employ a central potential consisting of the sum of attractive and repulsive Gaussians,

$$V_S(r) = -U_S \exp\left(-\frac{r^2}{\alpha_S^2}\right) + W_S \exp\left(-\frac{r^2}{\beta_S^2}\right), \quad (48)$$

and use the same parameter values as used in Ref. [23]. These values are listed in Table III. The authors of Ref. [23] also investigated more elaborate Λn interactions but obtained results very similar to those obtained with the simple form of Eq. (48).

It is useful to decompose the quantity Ψ defined by Eq. (45) into a plane wave piece and an interacting part,

$$\Psi_{M_\Lambda M_{nF} M'_\Lambda M'_{nF}}(\mathbf{p},\mathbf{q}) = (2\pi)^{3/2}\delta(\mathbf{p}-\mathbf{q})\delta_{M'_\Lambda M_\Lambda}\delta_{M'_{nF} M_{nF}} + \Phi_{M_\Lambda M_{nF} M'_\Lambda M'_{nF}}(\mathbf{p},\mathbf{q}), \quad (49)$$

where Φ, the interacting part, is given by the same expression as Ψ but with the full radial overlap function $R_{\ell S}$ replaced by

$$\tilde{\mathcal{R}}_{\ell S}(p,q) = \int_0^\infty r^2 dr \left[\frac{u_{\ell S}^*(p,r)}{r} - j_\ell(pr)\right] j_\ell(qr). \quad (50)$$

Even with the plane wave part removed, the numerical integration required to obtain $\tilde{\mathcal{R}}_{\ell S}$ does not converge when $q=p$. To circumvent this difficulty we divide the integrand of

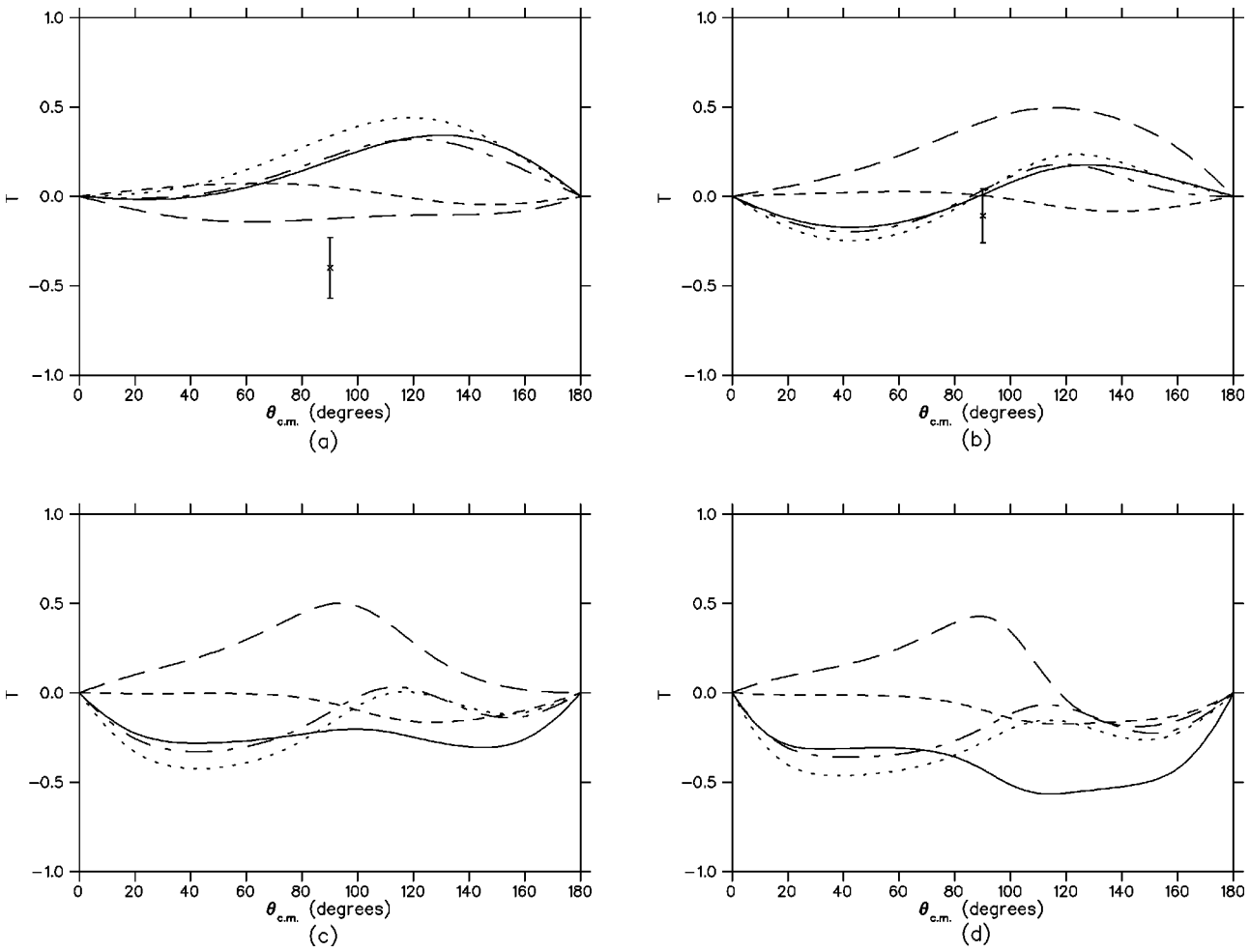

FIG. 6. Polarized proton target asymmetry for the reaction $\gamma p \to K^+\Lambda$ at (a) E_γ=1.1 GeV, (b) E_γ=1.3 GeV, (c) E_γ=1.55 GeV, and (d) E_γ=1.7 GeV. Identification of curves as in Fig. 4. The data points are from Ref. [40].

Eq. (50) into two parts, an asymptotic part, which can be integrated analytically, and the remainder, which has to be integrated numerically. This yields

$$\tilde{\mathcal{R}}_{\ell S}(p,q) = \tilde{\mathcal{R}}^{asy}_{\ell S}(p,q) + \tilde{\mathcal{R}}^{rem}_{\ell S}(p,q), \tag{51}$$

with

$$\tilde{\mathcal{R}}^{asy}_{\ell S}(p,q) = \frac{\exp(-i\delta_{\ell S})\sin\delta_{\ell S}}{q^2 - p^2 + i\epsilon}\left(\frac{\delta_{\ell,even}}{p} + \frac{\delta_{\ell,odd}}{q}\right), \tag{52}$$

where $\delta_{\ell S}$ is the Λn phase shift.

After constructing the radial integrals $\tilde{\mathcal{R}}_{\ell S}(p,q)$, it is still necessary to carry out the integration over **q** in Eq. (44). The angle integrals can be easily evaluated using a two dimensional Gauss points technique. The radial integrals require more care because of numerical instabilities associated with the denominator in Eq. (52). We have developed a numerical procedure that allows us to avoid these instabilities and to numerically take the limits of the integrals as the parameter ϵ approaches zero. We have checked that the procedure converges well and that it yields the correct result for a test integral that can be evaluated analytically.

IV. NUMERICAL RESULTS AND DISCUSSION

A. Results for the reaction $\gamma p \to K^+\Lambda$

Although reaction (1) has been the subject of numerous studies over the past several decades, there is still relatively little polarization data for this reaction. Moreover, the existing data are not always in agreement. Consequently, in generating fits to the photoproduction of strangeness from protons, we have concentrated on the unpolarized differential cross section. Our strategy is to produce several fits to the cross section data and then to compare the polarization observables obtained with those fits. Since the main interest here is the study of parameter dependence within a particular model, rather than the quantitative reproduction of data, we choose to fit empirical representations of the cross section data generated by the SAID facility [34], rather than fit the data directly. In particular, we fit the SAID cross sections for reaction (1) at laboratory photon energies of 1.1 GeV, 1.4 GeV, and 1.7 GeV as functions of the c.m. scattering angle. To measure the quality of our fits, we define a cumulative relative error parameter through the relation

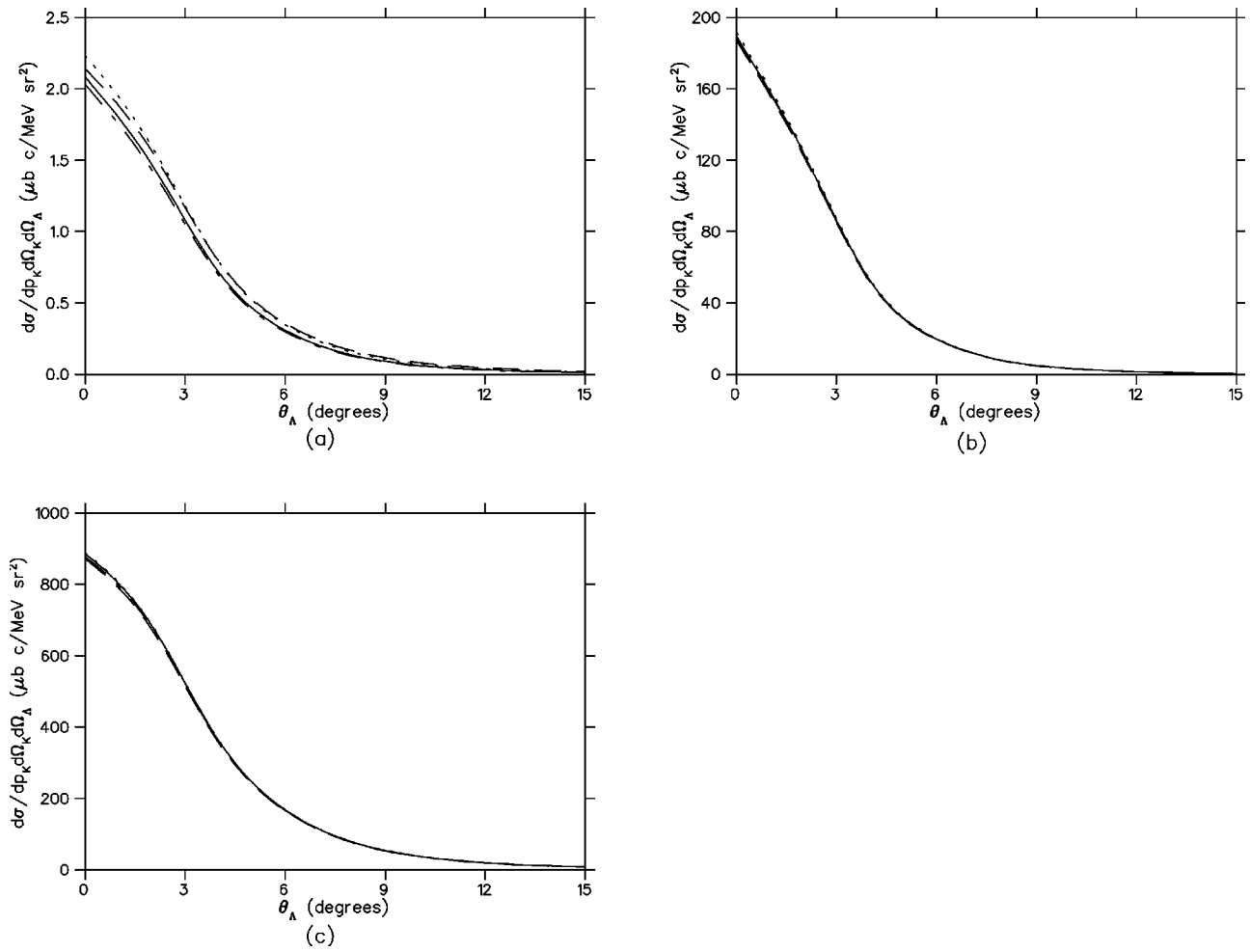

FIG. 7. Differential cross sections for the reaction $\gamma d \rightarrow K^+ \Lambda n$ at (a) $E_\gamma = 1.1$ GeV, $T_K = 325$ MeV, and $\theta_K = 15°$; (b) $E_\gamma = 1.4$ GeV, $T_K = 600$ MeV, and $\theta_K = 17°$; and (c) $E_\gamma = 1.7$ GeV, $T_K = 925$ MeV, and $\theta_K = 12°$. Identification of curves as in Fig. 2.

$$\chi^2 = \sum \frac{(d\sigma_{calc} - d\sigma_{emp})^2}{\overline{d\sigma^2}}, \tag{53}$$

where $d\sigma_{calc}$ is the calculated cross section at a particular energy and angle, $d\sigma_{emp}$ is the corresponding empirical cross section, and $\overline{d\sigma^2}$ is the angle average of $d\sigma^2_{emp}$ at each energy.

The resulting fits are presented in Table IV, which lists the coupling constant products defined by Eqs. (22) and (23) for the various resonances included in the fits. With the exceptions of fits E and F, all the fits here were obtained using the RS propagator for the spin $\frac{3}{2}$ resonances and the full, energy dependent resonance width prescription described in Sec. II. Fit E was obtained using the simplified width prescription in place of the full width prescription, while fit F was obtained using the ABW spin $\frac{3}{2}$ propagator in place of the RS propagator. Both spin $\frac{1}{2}$ and spin $\frac{3}{2}$ resonances were included in the *s* and *u*-channels of fits A, B, C, and E; whereas, in fits D and F, only spin $\frac{1}{2}$ resonances were incorporated in the *u*-channel. The two lowest χ^2 values, which are nearly identical, were achieved with fits A and E. The two highest values, also nearly identical, result from fits D and F.

Comparison of the various coupling products listed in Table IV makes it clear that cross section data alone do not constrain the coupling products very effectively. It is possible to achieve fits of comparable quality with quite different choices for the couplings of individual resonances. There are, however, some general trends in the fits that are worth noting. First, there are certain resonances that do not appear at all in the fits, namely, the $N(1710)$ and the $\Lambda(1520)$. Attempts to include either of these resonances lead to unacceptably large values of χ^2. Other resonances seem to require similar coupling product values in most of the fits. The $N(1440)$ coupling product, for example, is negative in all the fits and with the exception of fit E, tends to be large in magnitude. The $\Lambda(1670)$ coupling product, on the other hand, is either zero or very small in all the fits. Another interesting characteristic of the fits is that the *s*-channel spin $\frac{3}{2}$ resonances all have zero or very small values for the $G^2_{N\star}$ coupling product. Finally, it should be noted that there is a high degree of correlation among certain groups of couplings; i.e., an increase in one coupling can be nearly compensated by an increase or decrease in another coupling in the same group.

The quality of the various fits is exhibited in Fig. 2, which displays the differential cross sections obtained with fits A, B, C and D, and Fig. 3, which displays the differential cross sections obtained with fits A, E, D, and F. Although the vari-

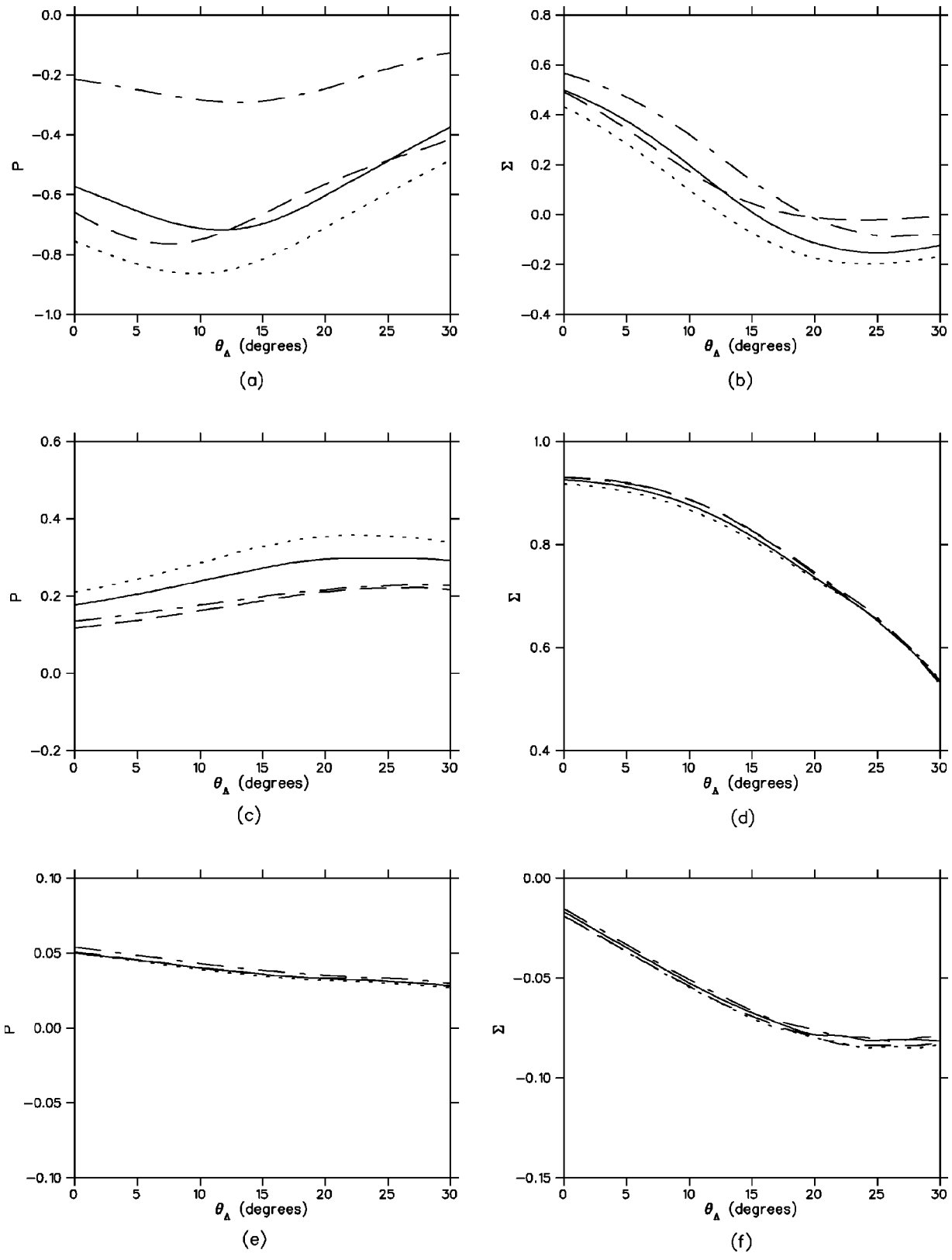

FIG. 8. Hyperon polarization asymmetry (left-hand panels) and polarized photon beam asymmetry (right-hand panels) for the reaction $\gamma d \rightarrow K^+ \Lambda n$ and the same kinematics as in Fig. 7. Identification of curves as in Fig. 2.

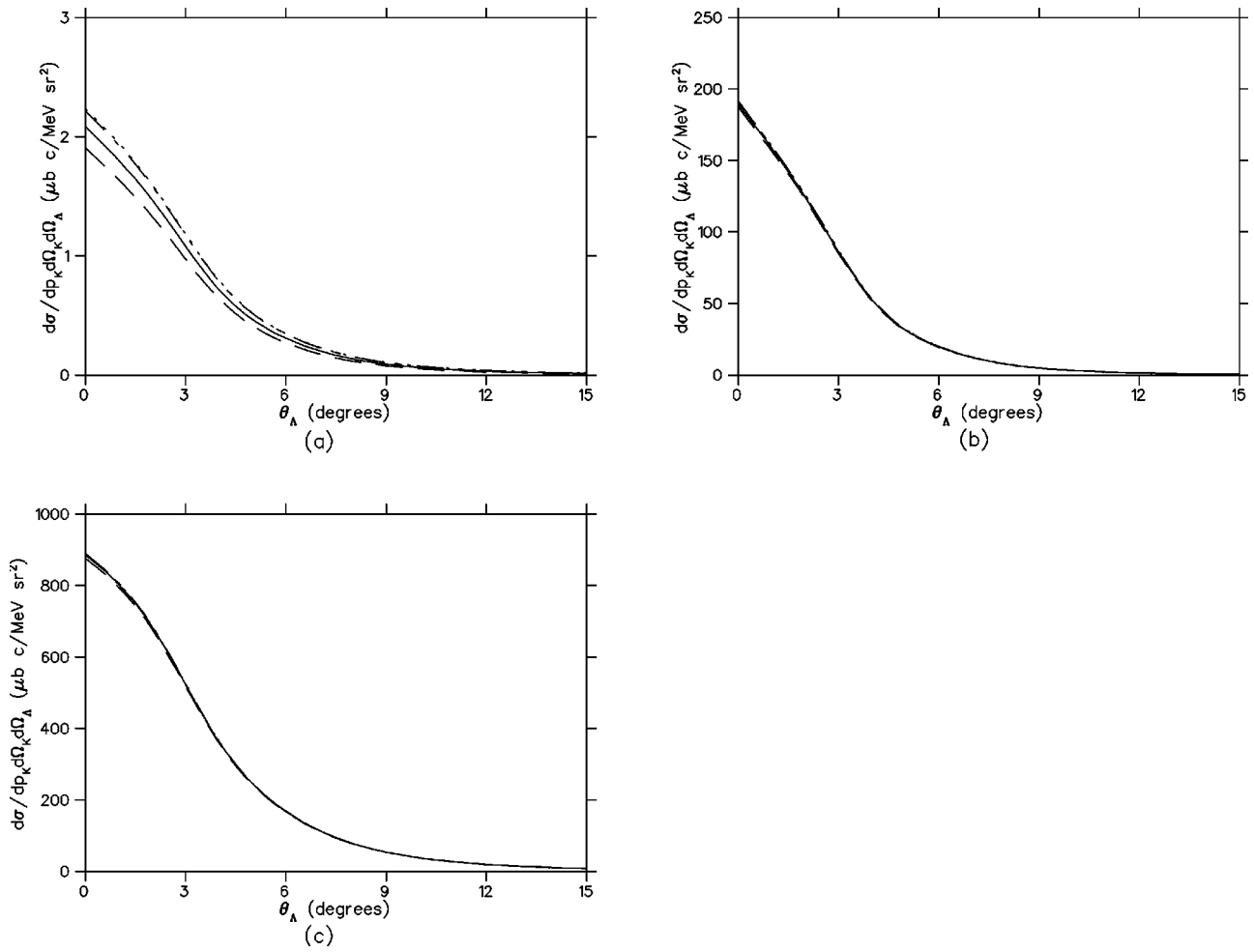

FIG. 9. Differential cross sections for the reaction $\gamma d \to K^+ \Lambda n$ and the same kinematics as in Fig. 7. Identification of curves as in Fig. 3.

ous parameter sets have different values of χ^2 associated with them, they all yield fits to the SAID curves of comparable quality. Note, however, that fits D and F, which do not incorporate spin $\frac{3}{2}$ resonances in the *u*-channel, are not quite as good as the other four fits. In Fig. 3, there is little difference between the solid and dashed curves and between the dotted and dot-dashed curves, indicating that different choices for the resonance width prescription and different choices for the spin $\frac{3}{2}$ propagator have little influence on the calculated cross sections.

Figures 4, 5, and 6 display results for the polarization parameters defined by Eqs. (31), (32), and (33) for several photon energies between 1.0 GeV and 1.75 GeV. In Fig. 4, the data points from Refs. [35–37] shown in panel (a) represent data taken at several energies between 1.00 GeV and 1.05 GeV, the data points from Refs. [38,39] shown in panel (b) represent data taken at 1.3 GeV, and the data point from Ref. [39] in panel (c) represents data taken at 1.5 GeV. The energies of the SAPHIR data points shown in Fig. 4 have not been determined precisely but only over ranges in energy that are centered at the energies listed for each panel. This is also true of the LEPS data points shown in panels (c) and (d) of Fig. 5.

These figures clearly show that similar cross section fits can yield quite different predictions for polarization observables. The hyperon polarization asymmetries obtained with fits A and B, for example, are quite dissimilar, even though the same resonance width and propagator prescriptions were employed in the two fits. The proton target asymmetries obtained with these two fits are also quite different. One rather surprising feature of the polarization results is the dissimilarity in the results obtained with fits A and E (solid and short dashed curves in the figures). These two fits differ in the width prescriptions employed but have almost identical χ^2 values. Evidently, the polarization observables obtained in effective Lagrangian models are rather sensitive to the treatment of the resonance widths. On the other hand, as a comparison of the dotted and dot-dashed curves reveals, the calculated polarization observables are not very sensitive to the form of the resonance propagator adopted, at least not in the absence of spin $\frac{3}{2}$ resonances in the *u*-channel.

A comparison of the calculated polarization observables with the data is not very encouraging. The calculated hyperon asymmetries all disagree with the SAPHIR data, particularly at back angles, where the SAPHIR values are positive and the calculated asymmetries generally zero or negative. At the highest photon energy considered, there is

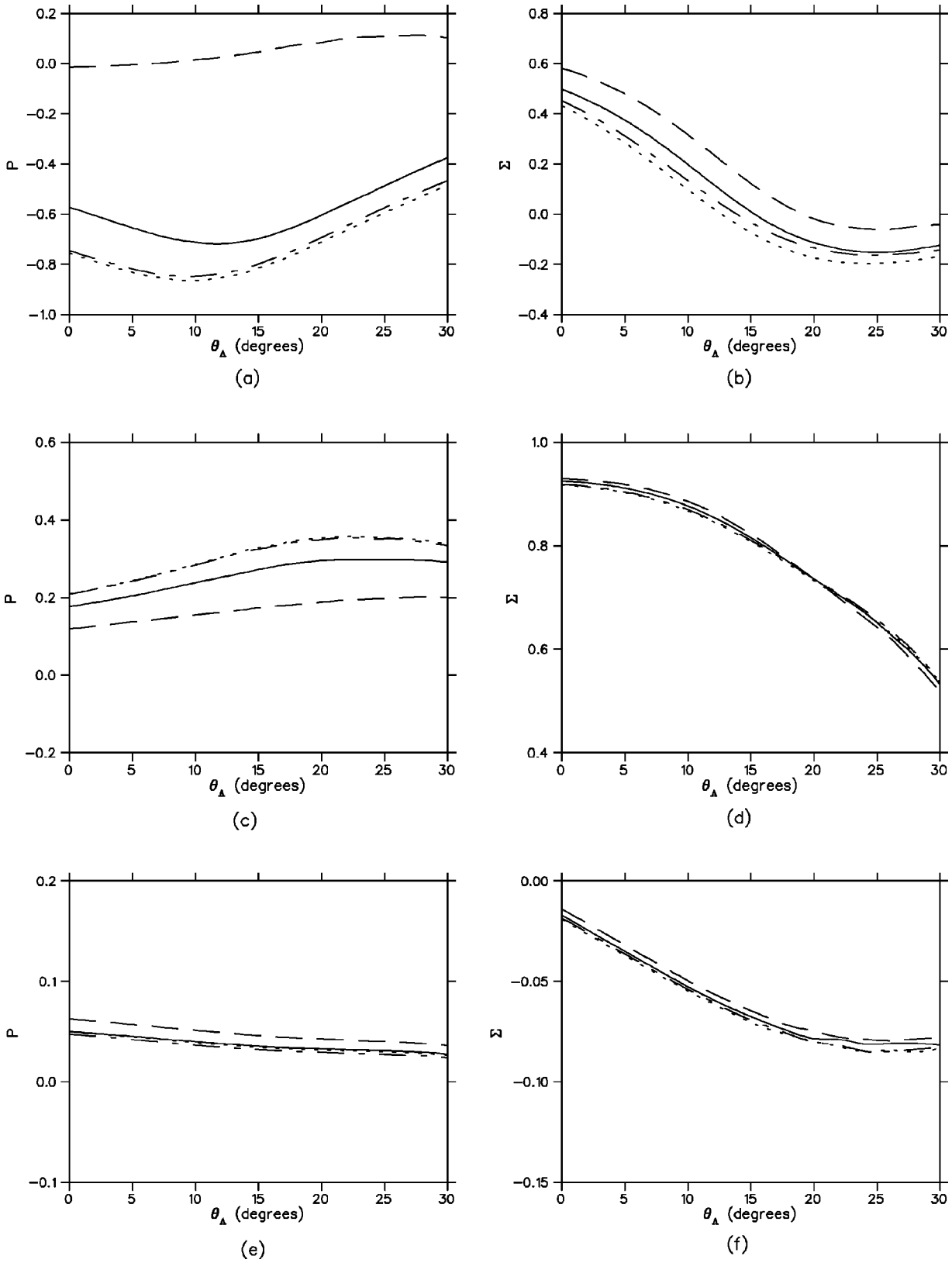

FIG. 10. Hyperon polarization asymmetry (left-hand panels) and polarized photon beam asymmetry (right-hand panels) for the reaction $\gamma d \rightarrow K^+ \Lambda n$ and the same kinematics as in Fig. 7. Identification of curves as in Fig. 3.

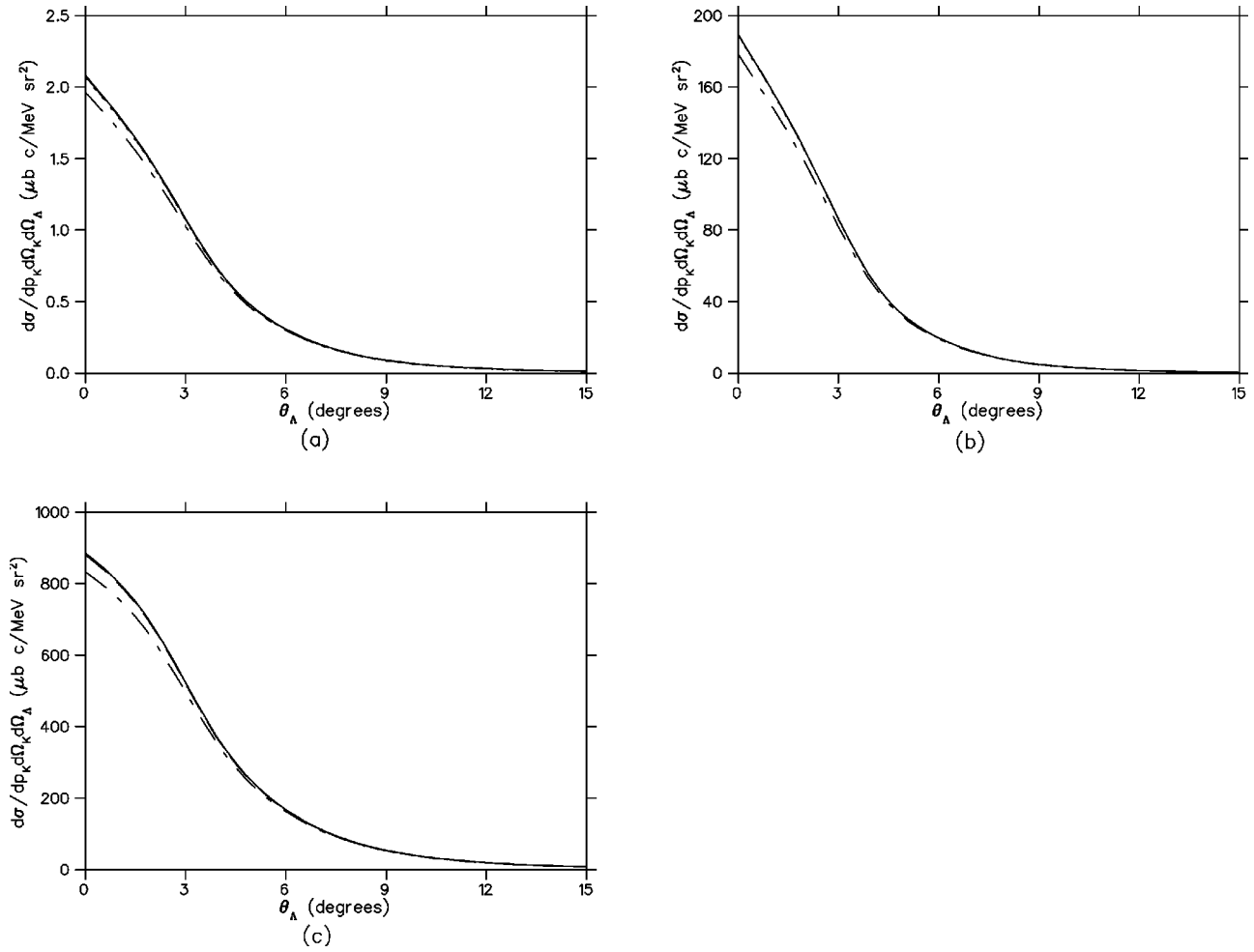

FIG. 11. Differential cross sections for the reaction $\gamma d \rightarrow K^+ \Lambda n$ and the same kinematics as in Fig. 7. The solid curves were obtained with final state interaction A, the long dashed curves with final state interaction B, the short dashed curves with final state interaction C, the dotted curves with no final state interaction, and the dot-dashed curves with the Reid deuteron wave function.

also disagreement between the LEPS data for the beam polarization asymmetry and our calculated values. The authors of Ref. [18] comment that their beam polarization results are not consistent with theoretical predictions based on tree-level effective Lagrangians. Our results seem to conform with this observation and may indicate a fundamental shortcoming of such approaches.

B. Results for the reaction $\gamma d \rightarrow K^+ \Lambda n$

The differential cross section defined by Eq. (42) for reaction (2) in the deuteron rest frame depends on five independent kinematic variables, which may be chosen as the incident photon energy E_γ, the kaon kinetic energy T_K, the kaon scattering angle θ_K defined relative to the photon beam direction, the Λ angle θ_Λ defined in the preceding section, and the angle ϕ between the plane containing the outgoing baryon momentum and the plane containing $\mathbf{p}_\gamma$ and $\mathbf{p}_\mathbf{K}$. Since the calculated observables depend rather weakly on this last observable, only results obtained with $\phi = 0$ will be reported here.

In Fig. 7 we present cross section results for the four resonance coupling fits displayed in Fig. 2. At each photon energy, the values for T_K and θ_K have been chosen to make the calculated cross sections lie close to the quasielastic peak where the reaction amplitude is well represented by the impulse approximation. All the results shown were obtained with the Paris deuteron wave function and a final state wave function generated from interaction model A in Table III. As is evident from the figure, the cross section is strongly forwarded peaked in θ_Λ for the kinematic choices considered, and there is very little dependence on the particular resonance fit employed, particularly at the two higher photon energies.

Corresponding results for the hyperon polarization asymmetry and the photon beam polarization asymmetry are displayed in Fig. 8. Except for the hyperon polarization at $E_\gamma = 1100$ MeV, the dependence on the particular resonance fit employed is considerably less here than for reaction (1). Even at $E_\gamma = 1100$ MeV, the shapes of the hyperon polarizations as functions of θ_Λ are similar for the four fits; only the overall polarization magnitudes are different. This suggests that polarization data taken with deuteron targets will be less valuable than that taken with proton targets for distinguishing between different Lagrangian model fits.

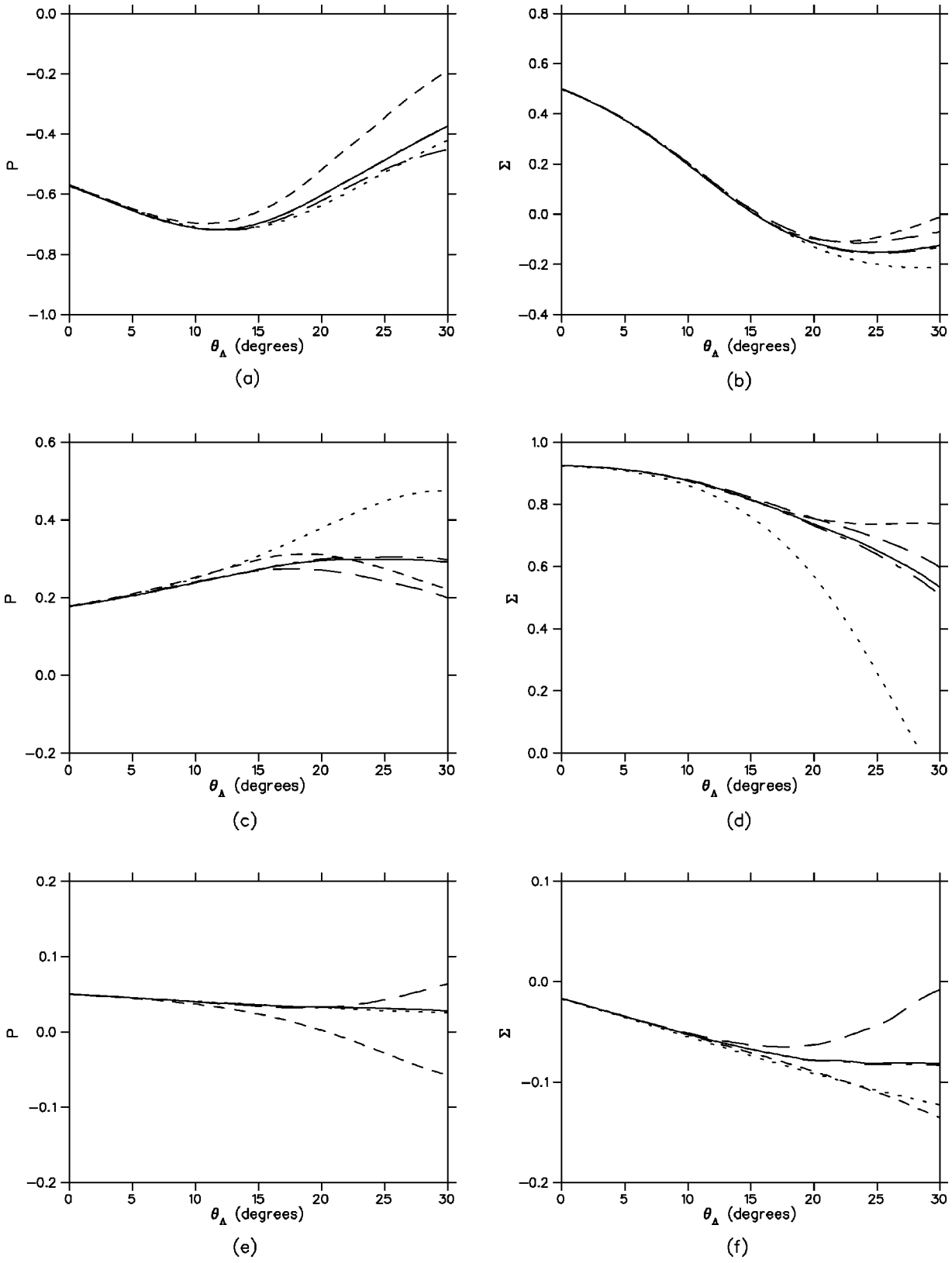

FIG. 12. Hyperon polarization asymmetry (left-hand panels) and polarized photon beam asymmetry (right-hand panels) for the reaction $\gamma d \rightarrow K^+ \Lambda n$ and the same kinematics as in Fig. 7. Identification of curves as in Fig. 11.

Figures 9 and 10 display cross section and polarization results for reaction (2) for the four resonance coupling fits presented in Fig. 3. Again, there is very little dependence exhibited in the cross sections on the particular resonance model employed. The polarization observables show greater resonance model dependence, but not as much as for the photoproduction of strangeness from protons. As for reaction (1), the most significant dependence is on the resonance width prescription (compare the solid and dashed curves), while the dependence on the resonance propagator prescription is much less important (dotted and dot-dashed curves).

In the last two figures, we explore the dependences of the calculated cross sections and polarization observables on the initial and final state wave functions. In these figures results are displayed for the three final state interaction models listed in Table III and for an initial deuteron wave function obtained from the Reid potential. Figure 11 reveals that the cross section has virtually no dependence on the final state interaction and depends only weakly on the deuteron wave function. The polarization observables, on the other hand, depend more strongly on the final state interaction than on the deuteron wave function, particularly away from forward values of θ_Λ. Unfortunately, the cross section drops so rapidly as θ_Λ increases that is doubtful whether the polarization observables can be measured precisely enough to distinguish between different final state interactions, at least for the kinematic choices considered here (see Fig. 12).

In summary, we have studied the model dependence of kaon photoproduction from both protons and deuterons within an effective Lagrangian model. The differential cross section and a number of single polarization observables have been examined at several different energies for both reactions. In the case of the proton reaction, we find that fitting the empirical cross sections does not constrain the calculated polarization observables very effectively. We find, moreover, that the polarization observables calculated for proton targets are quite sensitive to the manner in which the resonances widths are treated but relatively insensitive to the prescription used for the spin $\frac{3}{2}$ resonance propagators. Overall, our results indicate that the polarization observables calculated for deuteron targets are less model dependent than those calculated for proton targets. For the kinematics considered, we also find that the deuteron target results are not especially sensitive to either the deuteron wave function or the final state interaction.

[1] R.A. Adelseck, C. Bennhold, and L.E. Wright, Phys. Rev. C **32**, 1681 (1985); R. A. Adelseck and L.E. Wright, *ibid.* **38**, 1965 (1988).

[2] R.A. Adelseck and B. Saghai, Phys. Rev. C **42**, 108 (1990).

[3] Robert A. Williams, Chueng-Ryon Ji, and Stephen R. Cotanch, Phys. Rev. C **46**, 1617 (1992).

[4] T. Mart, C. Bennhold, and C.E. Hyde-Wright, Phys. Rev. C **51**, R1074 (1995); H. Haberzettl, C. Bennhold, T. Mart, and T. Feuster, *ibid.* **58**, R40 (1998); H. Haberzettl, C. Bennhold, and T. Mart, Acta Phys. Pol. B **31**, 2387 (2000).

[5] M.K. Cheoun, B.S. Han, B.G. Yu, and Il-Tong Cheon, Phys. Rev. C **54**, 1811 (1996); Bong Son Han, Myung Ki Cheoun, K.S. Kim, and Il-Tong Cheon, Nucl. Phys. **A691**, 713 (2001).

[6] J.C. David, C. Fayard, G.H. Lamot, and B. Saghai, Phys. Rev. C **53**, 2613 (1996).

[7] T. Mizutani, C. Fayard, G.-H. Lamot, and B. Saghai, Phys. Rev. C **58**, 75 (1998).

[8] S.S. Hsiao, D.H. Lu, and Shin Nan Yang, Phys. Rev. C **61**, 068201 (2000).

[9] Wen Tai Chiang, F. Tabakin, T-S.H. Lee, and B. Saghai, Phys. Lett. B **517**, 101 (2001).

[10] Stijn Janssen, Jan Ryckebusch, Wim Van Nespen, Dimitri Debruyne, and Tim Van Cauteren, Eur. Phys. J. A **11**, 105 (2001); Stijn Janssen, Jan Ryckebusch, Dimitri Debruyne, and Tim Van Cauteren, Phys. Rev. C **65**, 015201 (2002); S. Janssen, D.G. Ireland, and J. Ryckebusch, Phys. Lett. B **562**, 51 (2003); S. Janssen, J. Ryckebusch, and T. Van Cauteren, Phys. Rev. C **67**, 052201 (2003).

[11] Dinghui Lu, R.H. Landau, and S.C. Phatak, Phys. Rev. C **52**, 1662 (1995).

[12] V. Keiner, Z. Phys. A **352**, 215 (1995).

[13] Zhenping Li, Phys. Rev. C **52**, 1648 (1995); Zhenping Li, Ma Wei-Hsing, and Zhung Lin, *ibid.* **54**, R2171 (1996); Zhenping Li, Hongxing Ye, and Minghui Lu, *ibid.* **56**, 1099 (1997); M.H. Lu, W.X. Ma, B. Saghai, and Z.P. Li, High Energy Phys. Nucl. Phys. **22**, 255 (1998); L.J. Zhou, W.X. Ma, and G.X. Peng, *ibid.* **25**, 1051 (2001); L.J. Zhou, W.X. Ma, and G.X. Peng, Sci. China, Ser. A: Math., Phys., Astron. **45**, 671 (2002).

[14] S. Ahlig, R. Alkofer, C. Fischer, M. Oettel, and H. Reinhardt, Prog. Part. Nucl. Phys. **44**, 361 (2000); R. Alkofer, S. Ahlig, C. Fischer, and M. Oettel, Nucl. Phys. **A680**, 70c (2001).

[15] S. Steininger and U.-G. Meissner, Phys. Lett. B **391**, 446 (1997).

[16] N. Kaiser, T. Waas, and W. Weise, Nucl. Phys. **A612**, 297 (1997); J.C. Ramon, N. Kaiser, S. Wetzel, and W. Weise, *ibid.* **A672**, 249 (2000).

[17] M.Q. Tran *et al.*, Phys. Lett. B **445**, 20 (1998); S. Goers *et al.*, *ibid.* **464**, 331 (1999).

[18] R.G.T. Zegers *et al.*, Phys. Rev. Lett. **91**, 092001 (2003).

[19] G. Niculescu *et al.*, Phys. Rev. Lett. **81**, 1805 (1998); L. Teodorescu *et al.*, Nucl. Phys. **A658**, 362 (1999); R.M. Mohring *et al.*, Phys. Rev. C **67**, 055205 (2003).

[20] D.S. Carman *et al.*, Phys. Rev. Lett. **90**, 131804 (2003).

[21] F.M. Renard and Y. Renard, Nucl. Phys. **B1**, 389 (1967); Phys. Lett. **24B**, 159 (1967).

[22] R.A. Adelseck and L.E. Wright, Phys. Rev. C **39**, 580 (1989).

[23] Xiaodong Li and L.E. Wright, J. Phys. G **17**, 1127 (1991).

[24] H. Yamamura, K. Miyagawa, T. Mart, C. Bennhold, H. Haberzettl, and W. Glockle, Phys. Rev. C **61**, 014001 (1999).

[25] A.M. Boyarski, R. Diebold, S.D. Ecklund, G.E. Fischer, Y. Murata, B. Richter, and M. Sands, Phys. Lett. **34B**, 547 (1971); D.J. Quinn, J.P. Rutherford, M. A. Shupe, D. J. Sherden, R.H. Siemann, and C.K. Sinclair, Phys. Rev. D **20**, 1553 (1979).

[26] C.J. Bebek *et al.*, Phys. Rev. D **15**, 594 (1977).
[27] C. Caso *et al.*, Eur. Phys. J. C **3**, 1 (1998).
[28] David Faiman, Nucl. Phys. **B32**, 573 (1971); D. Faiman and D.E. Plane, *ibid.* **B50**, 379 (1972); D. Faiman, *ibid.* **B115**, 478 (1976).
[29] A.J.G. Hey, P.J. Litchfield, and R.J. Cashmore, Nucl. Phys. **B95**, 516 (1975).
[30] M. Benmerrouche, R.M. Davidson, and Nimai C. Mukhopadhyay, Phys. Rev. C **39**, 2339 (1989).
[31] V. Pascalutsa, Phys. Rev. D **58**, 096002 (1998); Nucl. Phys. **A680**, 76C (2001); Phys. Lett. B **503**, 85 (2001).
[32] J.J. de Swart, Rev. Mod. Phys. **35**, 916 (1963).
[33] Oren V. Maxwell, Phys. Rev. C **69**, 034605 (2004).
[34] CNS Data Analysis Center web site; John S. Hyslop, Richard A. Arndt, L. David Roper, and Ron L. Workman, Phys. Rev. D **46**, 961 (1992).
[35] H. Thom, E. Gabathuler, D. Jones, B.D. McDaniel, and W.M. Woodward, Phys. Rev. Lett. **11**, 433 (1963).
[36] M. Grilli, L. Mezzetti, M. Nigro, and E. Schiavuta, Nuovo Cimento **38**, 1467 (1965).
[37] T. Fujii *et al.*, Phys. Rev. D **2**, 439 (1970).
[38] D.E. Groom and J.H. Marshall, Phys. Rev. **159**, 1213 (1967).
[39] R. Hass, T. Miczaika, U. Opara, K. Quabach, and W.J. Schwille, Nucl. Phys. **B137**, 261 (1978).
[40] K.H. Althoff *et al.*, Nucl. Phys. **B137**, 269 (1978).